3D optimization of heat sink fins using adjoint-based optimization with a CAD-based parametrization

Pai Raikar, Praharsh; Anand, Nitish; Pini, Matteo; De Servi, Carlo

DOI
10.1016/j.ijheatmasstransfer.2025.127722

Publication date
2026

Document Version
Final published version

Published in
International Journal of Heat and Mass Transfer

International Journal of Heat and Mass Transfer 255 (2026) 127722

Contents lists available at ScienceDirect

International Journal of Heat and Mass Transfer

journal homepage: www.elsevier.com/locate/hmt

3D optimization of heat sink fins using adjoint-based optimization with a CAD-based parametrization

Praharsh Pai Raikar [a,b], Nitish Anand [a], Matteo Pini [b], Carlo De Servi [a,b,*]

[a] Flemish Institute for Technological Research (VITO), Boertang 200, Mol, 3600, Belgium
[b] Delft University of Technology, Kluyverweg 1, Delft, 2629HS, The Netherlands

ARTICLE INFO

Keywords:
Adjoint-based shape optimization
CAD parametrization
Heat sinks
Fin design

ABSTRACT

This study presents an automated shape optimization method for heat sinks. The computational framework has been developed by combining a conjugate heat transfer solver with adjoint capabilities, a CAD parametrization tool, and a gradient-based optimizer. The test case considers the design optimization of a water-cooled heat sink with pin fins, with the goal of concurrently enhancing heat transfer and minimizing pressure losses. Results show that the optimized fin geometry leads to an improvement of the average heat transfer coefficient by 24% while the pressure drop is lowered by 19%. The optimal fin array features an unconventional shape with an enlarged cross-section at the hub and the top with respect to mid-span, and a variation of the pin profile in the streamwise direction. The net effect is a reduction in flow blockage, an increase in fin efficiency, and a lower and more uniform temperature distribution in the heat sink base plate.

1. Introduction

The electrification of aircraft propulsion and power systems offers a promising solution for reducing carbon emissions in aviation [1]. However, to realize the potential of aircraft electrification, challenges related to the dissipation of thermal power generated by electric motors, batteries, and other electronic components must be addressed [2]. Thus, effective thermal management systems (TMS) are essential to enable the more electric aircraft of the future. The heat exchangers and heat sinks in such TMS must, therefore, be designed to handle significantly high thermal loads (estimated to be 2–10 kW/m^2 for batteries and 10–50 kW/m^2 for motors) while having minimum drag, low weight, and compact footprint [3].

The optimal design of heat exchangers and heat sinks of TMS is nowadays supported by high-fidelity numerical simulations, used either in parametric analyses or adopted in optimization studies [4]. The thermal–hydraulic performance of the components is evaluated with conjugate heat transfer (CHT) models, whereby relevant flow quantities (e.g., pressure drop, flow maldistribution) and heat transfer rates are predicted using three-dimensional RANS modeling [5], while the temperature distribution within the solid medium is determined by solving the energy equation [6].

Recently, the application of CHT models in parametric studies has led to the discovery of unconventional heat sink geometries with superior thermal–hydraulic performance. For example, Ahmadian-Elmi et al. [7] investigated the effect of pin fin geometric parameters — such as height, diameter, pitch, and taper angle — on the heat sink performance, defined as a function of the overall heat transfer coefficient and pressure drop. The results indicated that the fin shape has a major influence on the convective heat transfer coefficient and the pressure drop. More specifically, tapered pin fins showcased a performance improvement of 17% over conventional cylindrical pin fins. Similarly, Kim et al. [8] performed a parametric study to identify an optimum shape for the fins of the oil cooler of an aero gas-turbine engine. The fin geometry leading to the highest performance featured a forward-slanted profile that accelerated the flow near the bottom of the fin and enhanced local heat transfer. However, parametric studies such as the ones documented in Ref. [7,8] are impractical to explore comprehensively all the design options.

Optimized designs of heat transfer components can be achieved by coupling CHT simulations with an optimization algorithm. Two coupling strategies are generally pursued to limit the computational burden of the optimization problem. The first one requires the derivation of a surrogate of the CFD or CHT model of the heat transfer device under design. The optimization is then performed using a gradient-free evolutionary algorithm. The second strategy consists of directly coupling a 3D CHT model with a gradient-based optimization algorithm. The first approach provides a suitable trade-off between accuracy and computational cost for optimization problems with a number of design variables in the order of 10–20, as the computational time required to generate

* Corresponding author at: Delft University of Technology, Kluyverweg 1, Delft, 2629HS, The Netherlands.
E-mail address: c.m.deservi@tudelft.nl (C. De Servi).

https://doi.org/10.1016/j.ijheatmasstransfer.2025.127722
Received 1 April 2025; Received in revised form 23 July 2025; Accepted 17 August 2025
Available online 8 September 2025

Nomenclature

Symbols

a	Cross-sectional area [m^2]
A	Area [m^2]
c	Constraints
C_p	Specific heat capacity [$J/(kg\,K)$]
d	Pin fin diameter of the baseline heat sink [m]
D_h	Hydraulic diameter of the flow channel [m]
Eu	Euler number [–]
f	Fanning friction factor [–]
$\mathcal{G}$	Fixed-point iterators
h	Heat transfer coefficient [$W/(m^2\,K)$]
$\bar{h}$	Area averaged heat transfer coefficient [$W/(m^2\,K)$]
H	Height of the heat sink flow channel [m]
J	Objective function
k	Thermal conductivity [$W/(m\,K)$]
l	Projected length [m]
$\mathcal{L}$	Lagrangian function
L	Length of the heat sink [m]
$\mathcal{M}$	Mesh mapping operator
N	Number of sections [–]
p	Perimeter [m]
P	Pressure [Pa]
pt	Pitch of the heat sink fins [m]
q	Heat transfer rate [W]
r	Radius of curvature [m]
t	Thickness distribution [m]
T	Temperature [K]
U	Solution state
$\mathcal{V}$	Volume [m^3]
V	Velocity [m/s]
w	Plane perpendicular to the width
W	Width of the heat sink [m]
X	Mesh coordinates [m]
x, y, z	Cartesian coordinates [m]
y^+	Non-dimensional wall distance [–]

Greek letters

$\boldsymbol{\alpha}$	Design variables
$\lambda, \boldsymbol{\Phi}$	Lagrange multipliers / adjoint states
Δ	Change in quantities
η	Efficiency
μ	Viscosity [Pa s]
ρ	Density [kg/m^3]
θ	Metal angle [°]
ξ	Stagger angle [°]
ζ	Tangent proportion [–]

Subscripts

0	Baseline value
avg	Average value
b	Bottom heated surface
chord	Chord-wise
cht	Conjugate heat transfer
f	Fluid domain
fin	Fin
fr	Frontal
g	Geometric
i, j	Index
in	Inlet value
l	Lower bound
le	Leading edge
lg	Longitudinal
max	Maximum value
mean	Mean value
out	Outlet value
p	Location of pins
s	Solid domain
span	Span-wise
surf	Surface
t	Total
te	Trailing edge
tv	Transverse
u	Upper bound
ub	Unfinned base surface of the flow channel
vol	Volume
x	Component in x-direction
z	Zone

Superscripts

0	Iteration step 0
l	Lower
T	Transpose
u	Upper
*	Optimum value
$''$	Flux

the dataset for the implementation of the surrogate model significantly increases with the number of design variables. Hu et al. [9] optimized a 3D heat sink using a gradient-free method based on an evolutionary algorithm to reduce pressure drop along with temperature hotspots and non-uniformities. More recently, Nguyen et al. [10] utilized a surrogate model constructed with the machine-learning algorithm called random decision forests to optimize the three-dimensional shape of pin fins. The design variables consisted of the radii along the pin span, and the optimization resulted in funnel-shaped fins featuring a 20% higher heat transfer coefficient compared to the conventional cylindrical pins for the same pressure drop. Other studies have employed surrogate models based on artificial neural networks to design heat sinks with elliptical [11] and diamond-shaped [12] pin fins.

Gradient-based optimization methods with sensitivities obtained using the adjoint method are known to be very efficient for large-scale design problems with constraints [13]. In the context of shape optimization for conjugate heat transfer problems, Gkaragkounis et al. [14] developed a continuous adjoint CHT solver for turbulent flows and applied it to perform the 2D and 3D optimization of cooling channels of turbine blades and piston engines. Using the same adjoint-based computational framework, Gkaragkounis et al. [15] performed the multi-objective shape optimization of 3D heat sink fins, minimizing pressure drop and temperature hotspots. The result of the numerical exercise was a Pareto front constituted by a set of novel fin designs. Conversely, Anibal et al. [16] used the discrete adjoint formulation to compute the sensitivities and to carry out the optimal design of heat sinks for thermal management of electric motors in aerospace applications. The results highlighted the importance of modeling the thermal interaction between the solid and the fluid with a conjugate heat transfer solver, as opposed to approaches modeling the fluid

domain only. Similarly, Burghardt et al. [17] developed a discrete adjoint methodology for performing shape optimization in conjugate heat transfer problems, and implemented it leveraging the open-source software SU2. The method was applied to the optimal design of the 2D profile of a pin fin array and the cooling slots of a turbine blade. Recently, He et al. [18] applied discrete adjoint-based shape optimization to improve the cooling of battery cells. The CFD model domain encompassed an airflow channel and the aluminum casing surrounding each cell. To solve the corresponding aerothermal problem, a conjugate heat transfer analysis was performed by integrating a finite-volume fluid dynamics solver for the fluid domain with a conduction heat transfer solver for the solid domain, using the OpenMDAO-based MPhys framework. The optimized casing geometry reduces both the pumping losses associated with the airflow and the weight of the unit compared to the baseline cylindrical design, while still satisfying the constraints on the maximum temperature of the battery cells.

In all the aforementioned adjoint-based studies, the design surfaces were parametrized using methods based on Free-Form Deformation (FFD) boxes, which provide large design flexibility. However, parametrization based on FFD boxes does not easily allow imposing geometric constraints, such as those required for manufacturability [19,20]. In contrast, CAD-based parametrization with NURBS control points offers precise control and accurate representation of the design surface to define geometric constraints [21,22]. Yet, limited studies have focused on the application of CAD-based adjoint optimization in conjugate heat transfer problems. Chávez-Modena et al. [23] utilized a 2D parametrization based on control points to design a heat exchanger using a framework that sequentially optimizes the layout of the fins and then their shape. The optimized geometry was then extruded in 3D and simulated with a conjugate heat transfer solver, demonstrating a performance improvement of more than 10%. Imam-Lawal [24] optimized a U-bend internal cooling channel, whose thermal–hydraulic performance was computed with a CHT solver and its 3D geometry was parametrized by NURBS and rational Bezier curves. In a recent work, Pai Raikar et al. [25] proposed a CAD-based adjoint optimization framework to concurrently design multiple heat transfer surfaces and applied it to the optimal design of bare-tube heat exchangers, with the goal of minimizing pressure drop while constraining the heat transfer rate. However, the optimization framework in Ref. [25] neglected the modeling of the temperature distribution within the solid surfaces. In summary, the potential of CHT-based adjoint optimization for the optimal design of 3D heat transfer surfaces with CAD-based parametrization has not been investigated yet.

This study presents an adjoint-based optimization method relying on a conjugate heat transfer solver implemented in the open-source CFD software SU2 [26] and a CAD-based parametrization tool [27] based on NURBS to identify the optimal 3D shape of heat sinks. The objective is achieved by extending the automated design framework presented in Ref. [25] to conjugate heat transfer problems. The test case considered in this study involves the application of the shape optimization method to the design of a heat sink with pin fins, with the objective of concurrently maximizing the heat transfer coefficient and minimizing total pressure losses.

2. Methodology

The optimization framework integrates the open-source CFD software SU2 [26] for conjugate heat transfer simulation and gradient calculation with the discrete adjoint method, a mesh deformation algorithm, a CAD-based parametrization tool [27,28], and a gradient-based optimizer.

The XDSM diagram as shown in Fig. 1 illustrates the optimization framework. The framework is similar to the one reported in Ref. [25], with the addition of conjugate heat transfer (CHT) simulation capabilities, leveraging the partitioned approach in SU2, whereby the solid and the fluid domains are discretized with two distinct grids. In the design chain, the heat transfer design surfaces, such as pin fins, are parametrized by a set of design variables ($\boldsymbol{\alpha}$). The design surfaces at the interface of the fluid and solid domain, i.e. $\mathbf{X}_{\text{surf,f}}$ and $\mathbf{X}_{\text{surf,s}}$, respectively, are updated at each design iteration. The corresponding volume meshes $\left(\mathbf{X}_{\text{vol,f}}, \mathbf{X}_{\text{vol,s}}\right)$ are obtained by deforming the initial grids, i.e., those generated for meshing the solid and fluid domain. CHT simulation is performed with SU2 to compute the values of the objective function (J) and constraints ($\mathbf{c}$). Next, the adjoint variables $\left(\boldsymbol{\Phi}_{\text{f}}, \boldsymbol{\Phi}_{\text{s}}\right)$ are computed using the coupled CHT adjoint solver. Finally, the gradient values of the cost functions with respect to the design variables ($\boldsymbol{\alpha}$) are computed by applying the chain rule of differentiation, described in Section 2.3.

The gradient-based optimizer used in the design chain is the Sparse Nonlinear OPTimizer (SNOPT) [29], which is interfaced by means of the open-source python package *pyOptSparse* [30]. Mesh deformation is performed for each domain by solving the linear elasticity equations [31] with the surface displacements of the corresponding design surfaces imposed as a Dirichlet boundary condition. For brevity, only the methods at the basis of the functional blocks concerning 3D CHT problems, namely, the Geometry Modeler, the CHT Solver, and the Coupled Adjoint Solver, are described in detail. Further details are documented in Ref. [25,27].

Table 1
Design variables needed for the three-dimensional parametrization of fin surfaces with the camber-thickness approach.

Variable name	Symbol
Number of span-wise sections	N_{span}
Number of chord-wise sections	N_{chord}
Leading edge control points	$x_{\text{le}}, z_{\text{le}}$
Leading edge abscissa	y_{le}
Trailing edge control points	$x_{\text{te}}, z_{\text{te}}$
Stagger angle	ξ
Inlet and exit metal angles	$\theta_{\text{in}}, \theta_{\text{out}}$
Inlet and exit tangent proportions	$\zeta_{\text{in}}, \zeta_{\text{out}}$
Inlet and exit radii of curvature	$r_{\text{in}}, r_{\text{out}}$
Upper and lower thickness distributions	$t^{\text{u}}, t^{\text{l}}$

2.1. Geometry modeler

The CAD-based parametrization method from Ref. [27] is applied to model 3D geometries of heat transfer surfaces such as fins. The parametrization method enables the construction of a variety of geometries with NURBS surfaces that satisfy G-2 continuity. Fig. 2 illustrates the geometry construction method for an exemplary pin fin: a design surface is characterized by two independent thickness distributions imposed perpendicular to a camber surface. The camber surface is defined as a bi-quartic B-Spline surface [32] defined by a set of control points, the number of which can be selected based on the complexity of the geometry. Likewise, the thickness distributions determine the upper and lower profiles built around that camber surface. These profiles are defined using fourth-order B-spline surfaces whose parameters are listed in Table 1. The sensitivities of a pin surface with respect to the design variables are computed using the second-order accurate complex-step method. The equations defining the surfaces parametrized through the CAD modeler are documented in Ref. [27]. These analytical expressions are also used to compute the values of the geometric constraints ($\mathbf{c}_{\text{g}}$) and their sensitivities $\left(\frac{\mathrm{d}\mathbf{c}_{\text{g}}}{\mathrm{d}\boldsymbol{\alpha}}\right)$. The adopted CAD parametrization method is suitable for modeling geometries such as cylindrical, elliptical, and tapered fins, as well as unconventional heat transfer surfaces like teardrop and airfoil-type profiles, including three-dimensional variations of these shapes. However, it should be noted that this method is not applicable for parameterizing the geometry of perforated pins, wavy or louvered fins, and more complex topological structures such as fractal fins.

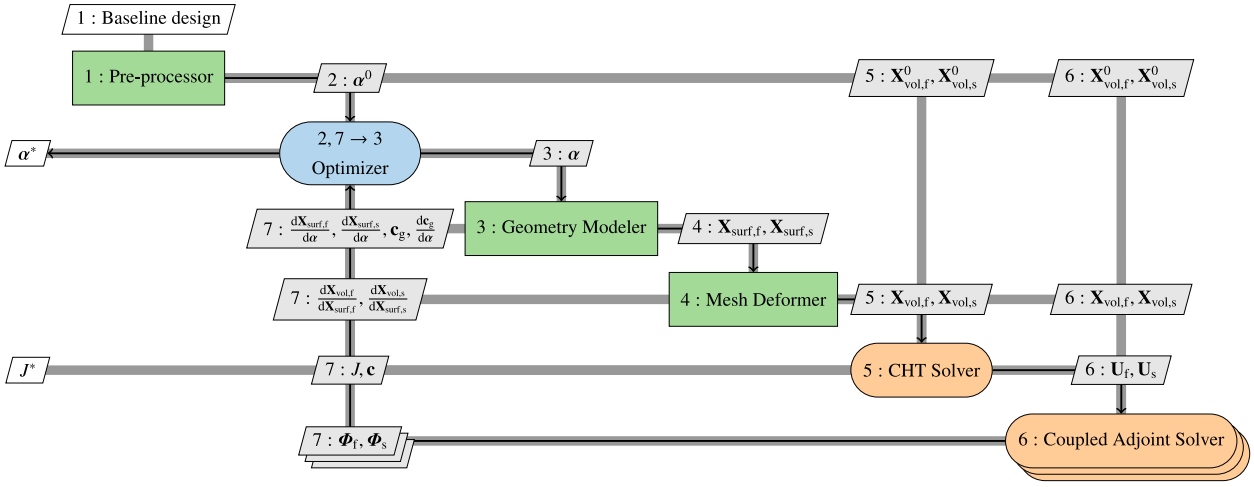

Fig. 1. XDSM diagram depicting the inter-dependencies among the blocks of the optimization framework.

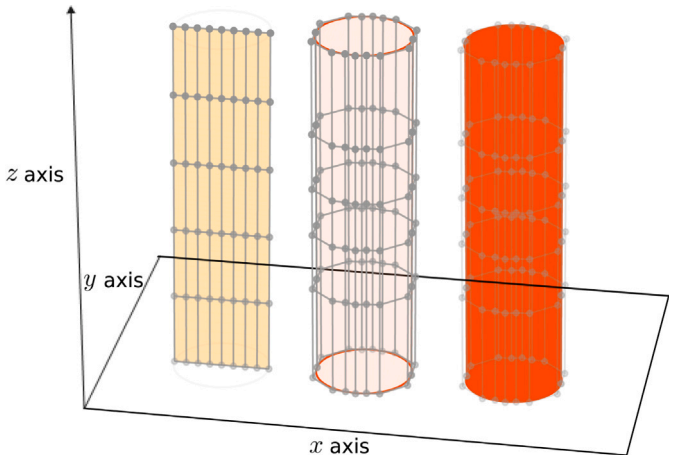

Fig. 2. Construction of the 3D geometry of an exemplary pin fin using the camber-thickness CAD parametrization approach. The camber surface (left) is characterized by the design variables associated with the coordinates of its control points, in particular those at the leading and trailing edge $(x_{le}, z_{le}, y_{le}, x_{te}, z_{te})$. The thickness distributions (t^u, t^l) determine the control points of the lower and upper pin profiles (middle) that characterize the overall design surface (right).

2.2. CHT solver

The conjugate heat transfer analyses are performed leveraging the partitioned approach in SU2 for solving coupled solid–fluid problems. In this approach, the flow is simulated with incompressible RANS, while heat conduction within the solid is computed by solving the energy equation. At the interface between the fluid and solid domain, the coupling conditions are represented by a Dirichlet boundary condition in the fluid domain, which prescribes a temperature equal to that of the solid at the interface, and the Robin boundary condition in the solid domain, which sets a heat flux proportional to a priori heat transfer coefficient and a temperature difference between the fluid and solid side [33]. The discretized form of the equations is obtained using the finite volume method with various numerical schemes available within SU2, as reported in Ref. [34]. The CHT solution state $\mathbf{U} = (\mathbf{U}_f, \mathbf{U}_s)$ is obtained using the block-Gauss–Sieldel algorithm till convergence is reached for the coupled system.

2.3. Coupled adjoint solver

The gradient computation is performed by using a discrete adjoint method for the coupled system, developed using the reverse mode of the open-source algorithmic differentiation tool CoDiPack [35]. The adjoint equations are solved using the same discretization schemes as those used in the primal solver, and their solutions exhibit similar convergence behavior as that of the flow equations.

To compute the sensitivities of the cost functions $(J, \mathbf{c})$ with respect to the design variables $(\boldsymbol{\alpha})$, the optimization problem can be expressed (similar to Ref. [36,37]) in the Lagrangian formulation as

$$\begin{aligned}\mathcal{L}(\boldsymbol{\alpha}, \mathbf{X}_{\text{vol,f}}, \mathbf{X}_{\text{vol,s}}, \mathbf{U}_f, \mathbf{U}_s, \boldsymbol{\lambda}_f, \boldsymbol{\lambda}_s, \boldsymbol{\Phi}_f, \boldsymbol{\Phi}_s) &= J(\mathbf{X}_{\text{vol,f}}, \mathbf{X}_{\text{vol,s}}, \mathbf{U}_f, \mathbf{U}_s) \\ &+ \boldsymbol{\lambda}_f^T[\mathcal{G}_f(\mathbf{X}_{\text{vol,f}}, \mathbf{U}_f, \mathbf{U}_s) - \mathbf{U}_f] + \boldsymbol{\lambda}_s^T[\mathcal{G}_s(\mathbf{X}_{\text{vol,s}}, \mathbf{U}_f, \mathbf{U}_s) - \mathbf{U}_s] \\ &+ \boldsymbol{\Phi}_f^T[\mathcal{M}_f(\boldsymbol{\alpha}) - \mathbf{X}_{\text{vol,f}}] + \boldsymbol{\Phi}_s^T[\mathcal{M}_s(\boldsymbol{\alpha}) - \mathbf{X}_{\text{vol,s}}],\end{aligned} \tag{1}$$

where $\mathbf{U} = (\mathbf{U}_f, \mathbf{U}_s)$ represents the solution state defined by the fixed-point iterators $\mathcal{G}_f$ and $\mathcal{G}_s$, $\mathcal{M}_f$ and $\mathcal{M}_s$ are the mesh mapping operators. Finally, the Lagrange multipliers (adjoint states) are represented by $\boldsymbol{\lambda}_f, \boldsymbol{\lambda}_s, \boldsymbol{\Phi}_f, \boldsymbol{\Phi}_s$, where the subscript denotes the zone index.

By following the derivation approach documented in Ref. [36] and differentiating the Lagrangian function $(\mathcal{L})$ with respect to its variables, the adjoint equations can be derived as

$$\boldsymbol{\lambda}_j^T = \frac{\partial J}{\partial \mathbf{U}_j} + \sum_{i=f,s} \boldsymbol{\lambda}_i^T \frac{\partial \mathcal{G}_i}{\partial \mathbf{U}_j} \quad \text{for } j = f, s, \tag{2}$$

$$\boldsymbol{\Phi}_j^T = \frac{\partial J}{\partial \mathbf{X}_{\text{vol},j}} + \boldsymbol{\lambda}_j^T \frac{\partial \mathcal{G}_j}{\partial \mathbf{X}_{\text{vol},j}} \quad \text{for } j = f, s, \tag{3}$$

where the adjoint states account for the coupling of physics in the fluid and solid domains. The solution to Eq. (2) can be obtained by following the iterative approach documented in Refs. [17,37]. The gradient of the objective function with respect to the design variables is obtained by

$$\frac{dJ}{d\boldsymbol{\alpha}} = \boldsymbol{\Phi}_f^T \frac{d\mathcal{M}_f}{d\boldsymbol{\alpha}} + \boldsymbol{\Phi}_s^T \frac{d\mathcal{M}_s}{d\boldsymbol{\alpha}}. \tag{4}$$

The total derivative of the mesh mapping operator for each zone with respect to the design variables can be calculated using the chain rule as

$$\frac{d\mathcal{M}}{d\boldsymbol{\alpha}} = \frac{d\mathbf{X}_{\text{vol}}}{d\mathbf{X}_{\text{surf}}} \cdot \frac{d\mathbf{X}_{\text{surf}}}{d\boldsymbol{\alpha}}, \tag{5}$$

where $\frac{d\mathbf{X}_{\text{vol}}}{d\mathbf{X}_{\text{surf}}}$ is the sensitivity of the volume mesh coordinates with respect to the surface coordinates and $\frac{d\mathbf{X}_{\text{surf}}}{d\boldsymbol{\alpha}}$ represents the sensitivity of the surface coordinates with respect to the design variables. Thus, the

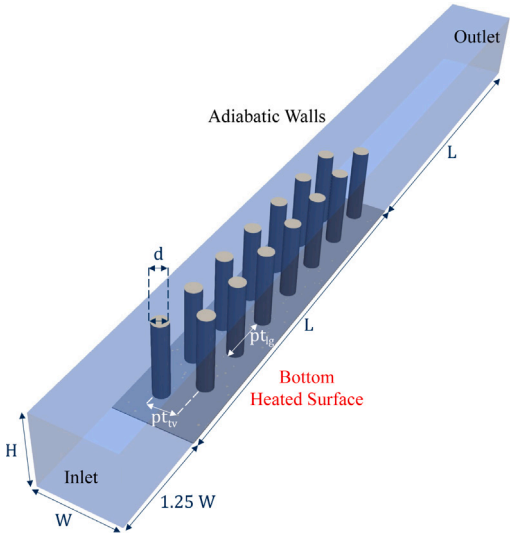

Fig. 3. Computational domain (with boundary markers and geometry parameters) corresponding to the baseline design.

Table 2
Geometry parameters defining the configuration of the heat sink.

Parameter	Description	Value [$\times 10^{-3}$ m]
d	Pin fin diameter	4.0
H	Height	20.0
W	Width	20.0
L	Length	100.0
pt_{lg}	Longitudinal pitch	13.0
pt_{tv}	Transverse pitch	7.0

sensitivity of the objective function with respect to the design variables can be computed as

$$\frac{dJ}{d\boldsymbol{\alpha}} = \boldsymbol{\Phi}_f \cdot \frac{d\mathbf{X}_{vol,f}}{d\mathbf{X}_{surf,f}} \cdot \frac{d\mathbf{X}_{surf,f}}{d\boldsymbol{\alpha}} + \boldsymbol{\Phi}_s \cdot \frac{d\mathbf{X}_{vol,s}}{d\mathbf{X}_{surf,s}} \cdot \frac{d\mathbf{X}_{surf,s}}{d\boldsymbol{\alpha}}. \tag{6}$$

3. Case study

The automated design framework is applied to the shape optimization of a heat sink with pin fins. This case study is inspired by Ref. [10], where pin fin shapes are optimized to enhance the thermal–hydraulic performance of a water-cooled heat sink subjected to a uniform heat flux at its bottom plate.

3.1. Heat sink geometry

The baseline geometry of the heat sink consists of two rows of cylindrical pin fins in a staggered arrangement, with each row consisting of 7 pins. Fig. 3 illustrates the heat sink geometry, and its dimensions are listed in Table 2.

3.2. Numerical model

Conjugate heat transfer simulation is performed on the computational domain shown in Fig. 3. A uniform velocity of 0.13 m/s and a temperature of 300 K are prescribed at the inlet boundary of the fluid domain. A gauge pressure of 0 Pa is imposed at the outlet boundary, implying atmospheric pressure conditions. No-slip condition is prescribed at the interface between the fluid and the solid domain through the CHT coupling described in Section 2.2. A uniform heat flux (q_b'') of 50,000 W/m^2 is applied to the bottom heated surface, which corresponds to an overall heat load of 100 W. The rest of the walls

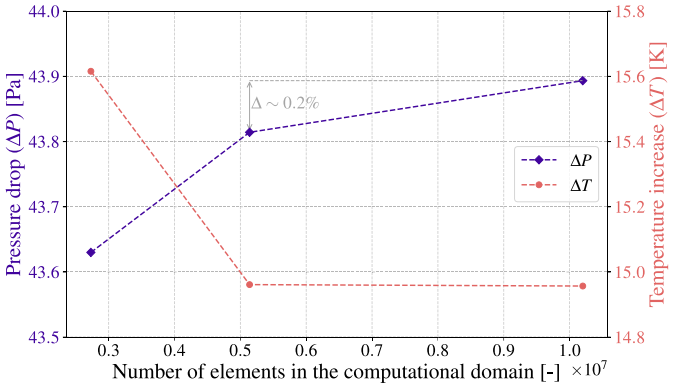

Fig. 4. Variation of performance parameters with mesh density.

are modeled as adiabatic surfaces. The material properties of water in the fluid domain and aluminum in the solid domain are assumed to be constant and are reported in Table 3.

The flow conditions correspond to a Reynolds number of about 3050, considering the hydraulic diameter of the flow channel

$$D_h = \frac{4WH}{2(W+H)}, \tag{7}$$

as the characteristic length. The turbulence is modeled using the one-equation Spalart–Allmaras model, which has a proven accuracy for heat transfer problems in internal flows [38].

The convective fluxes were reconstructed using the Flux-Difference-Splitting scheme with the MUSCL approach for second-order accuracy in the discretized form of the flow equations. The scalar upwind method was used for the convective fluxes of the turbulent equations. The Green–Gauss method was used to compute the spatial gradients for both solid and fluid domains. The steady-state solutions were obtained using a time-marching method using the Euler implicit time integration, with a CFL of 40. The linearized governing equations of the coupled system were solved using the FGMRES method with ILU preconditioning [34]. The maximum number of iterations per cycle of the linear solver for the fluid domain was 10 with a convergence tolerance of 10^{-4}, while for the solid domain, their values were 5 and 10^{-15}. To obtain the coupled solutions using the block-Gauss–Seidel algorithm, 12 000 iterations were performed. This setup achieved a residual reduction of 10 orders of magnitude for the pressure and velocity state variables, and 5 orders of magnitude for the temperature variables in both fluid and solid domains. Although further residual reduction could be obtained with additional iterations, the limit of 12 000 iterations was chosen as a trade-off between computational cost and solution accuracy. With this setting, a Cauchy convergence criterion of 10^{-7} was satisfied for all relevant thermal–hydraulic quantities.

3.3. Grid independence study and model validation

To perform the grid independence study, three hybrid unstructured meshes, consisting of hexahedral and prismatic elements, were generated using a commercial meshing tool [39]. The 3D meshes were generated by extruding 2D meshed surfaces along the height of the domain following a non-uniform progression as shown in Fig. 5. In the fluid domain, the hexahedral elements are clustered around the walls to ensure y^+ values of less than 1. The mesh refinement was performed by following a consistent approach that led to approximately doubling the total number of mesh elements across different meshes while keeping the inflation layer thickness and its progression fixed.

The variation of the relevant thermal–hydraulic quantities — temperature increase (ΔT) and pressure drop (ΔP) — with mesh density was investigated in the grid independence study. The temperature increase

Table 3
Thermo-physical properties of water and aluminum.

Material	Density (ρ) [kg/m^3]	Specific heat (C_p) [J/(kg K)]	Viscosity (μ) [Pa s]	Thermal conductivity (k) [W/(m K)]
Water	997	4182	0.85×10^{-3}	0.6
Aluminum	2700	897	–	237

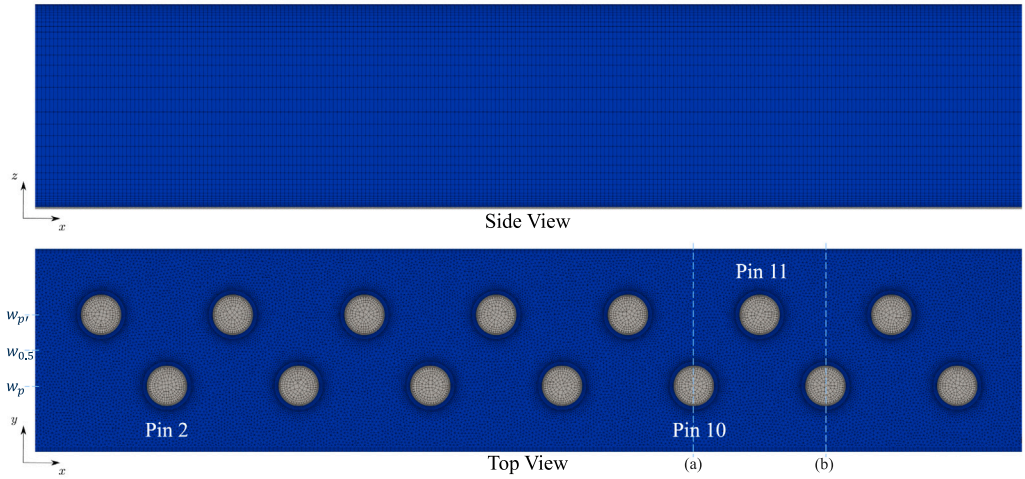

Fig. 5. Discretized computational domain selected from the grid independence study. The side view illustrates the height-wise progression of the extruded 2D mesh shown in the top view. The labels correspond to the pin index as well as the locations of the cross-sections used for data visualization.

(ΔT) is computed as the difference between the average temperature of the heated surface (T_{avg}) and the free-stream fluid temperature and is given by

$$\Delta T = T_{avg} - T_{in}, \tag{8}$$

where T_{in} is the water temperature at the inlet, and it approximates the free-stream temperature since the increase in water temperature in the flow domain is rather limited. Hence, ΔT can be related to the average heat transfer coefficient of the heat sink when applying constant heat flux. Lower values of ΔT and T_{avg} correspond to a higher convective heat transfer coefficient. Furthermore, the so-called pumping losses are estimated from the pressure drop computed by

$$\Delta P = P_{in} - P_{out}. \tag{9}$$

The variation of ΔT and ΔP is depicted in Fig. 4, which shows a monotonic convergence of their values with the increase in mesh density. It can be observed that the mesh consisting of 5.1 million elements resulted in a deviation of approximately 0.18% and 0.03% in ΔP and ΔT values, compared to the finest mesh. Therefore, the mesh of 5.1 million elements (shown in Fig. 5) was selected for the optimization study.

Additionally, the values of ΔP and ΔT obtained using the grid-independent mesh were compared with the experimental results derived from Ref. [40]. The comparison showed good agreement, with the results from the numerical model falling within the experimental uncertainty band of 4%.

3.4. Optimization problem

The goal of the optimization study is to simultaneously increase the heat transfer coefficient and reduce the pumping losses. Thus, the optimization objective is expressed in terms of minimization of the temperature increase and the pressure drop across the heat sink. The optimization problem can then be formulated as

$$\min_{\boldsymbol{\alpha}} \quad 0.8\frac{\Delta T(\boldsymbol{\alpha})}{\Delta T_0} + 0.2\frac{\Delta P(\boldsymbol{\alpha})}{\Delta P_0}, \tag{10}$$

$$\text{subject to} \quad \boldsymbol{\alpha}_l \le \boldsymbol{\alpha} \le \boldsymbol{\alpha}_u, \tag{11}$$

where $\boldsymbol{\alpha}$ represents the design variables, ΔP and ΔT are calculated using Eqs. (8) and (9) respectively, and the subscript 0 represents their values obtained with the baseline geometry. The values of the weights in the objective function were selected according to Ref. [10]. This choice was validated through a preliminary parametric study which revealed that to achieve a balanced improvement in both thermal and hydraulic performance, a higher weighting factor for ΔT is necessary.

The design variables ($\boldsymbol{\alpha}$) are the CAD parameters of the geometry of the fins that define the thickness distributions around the camber surface (t^u, t^l) and x-coordinates of the leading and trailing edges (x_{le}, x_{te}). The verification of the gradient of the objective function with respect to the design variables is documented in Appendix A. Bounds are imposed on the design variables such that the variation of the design surface is within a radial distance of 1 to 3 $\times 10^{-3}$ m from the center of the cylindrical pins of the baseline geometry. Specifically, the bounds on t^u, t^l are $\left[\frac{d}{4}, \frac{3d}{4}\right]$, and those on x_{le}, x_{te} are $\left[x_0 - \frac{0.45d}{2}, x_0 + \frac{0.45d}{2}\right]$, where x_0 denotes their corresponding baseline values and d is the pin fin diameter (see Table 1). These bounds on the design variables reflect minimum wall thickness constraints and are also informed by the limitations of the mesh deformation algorithm in maintaining acceptable mesh quality. To obtain fins with identical shapes, the sensitivities of the design variables corresponding to different pins were averaged using the CP-AS approach documented in Ref. [25]. Additionally, geometric symmetry of the fins was ensured by averaging the sensitivities corresponding to the design variables of the upper and lower thickness distributions, as also done in Ref. [25].

4. Results

Fig. 6 depicts the evolution of the objective function with the design iterations. The optimization leads to ~20% reduction in the value of the objective function in 37 design steps. This performance improvement is achieved by a simultaneous reduction in pressure drop and a reduction in the average temperature of the bottom part of the heat sink. In particular, the optimized geometry features an 18.8% lower pressure

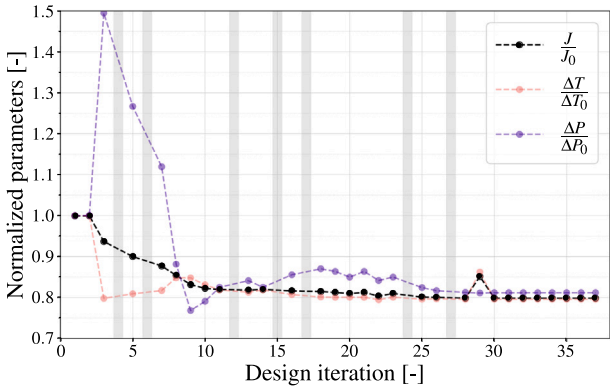

Fig. 6. Evolution of the normalized objective function and performance parameters with design iterations. The design iterations that led to a divergence of the CHT solver due to poor mesh quality are indicated by ▯ in the optimization history.

Table 4
Comparison of average heat transfer coefficient ($\bar{h}$), Fanning friction factor (f) and fin efficiency (η_{fin}) estimated for the baseline and optimized geometries.

	Units	Baseline	Optimized
$\bar{h}$	W/(m^2 K)	2133	2647
f	–	0.26	0.21
η_{fin}	–	0.37	0.44
$A_{\text{surf,t}}$	m^2	0.00352	0.00347
A_{ub}	m^2	0.00182	0.00165

drop with a 3 K lower average temperature of the heated surface (corresponding to 20.5% lower ΔT defined by Eq. (8)). The optimization process reduced the optimality, defined as the degree of satisfaction of the first-order Karush–Kuhn–Tucker conditions computed by SNOPT, by 2 orders of magnitude and the L2 norm of the gradient by 78%. Each primal and adjoint evaluation required ~2 hours with 222 cores and 444 GB of memory on a high-performance computing platform equipped with *Intel Xeon E5-2680v4* having 2.8 GHz clockspeed.

The average heat transfer coefficient ($\bar{h}$) and Fanning friction factor (f) corresponding to the baseline and optimized geometries are reported in Table 4. The average heat transfer coefficients for the finned heat sinks are computed using

$$\bar{h} = \frac{q''_{\text{b}} A_{\text{b}}}{(A_{\text{ub}} + \eta_{\text{fin}} A_{\text{surf,t}})\Delta T}, \tag{12}$$

where A_{b} is the area of the bottom heated surface, A_{ub} is the unfinned area of the base exposed to convection, $A_{\text{surf,t}}$ is the total surface area of all the fins, and η_{fin} is the fin efficiency. To compute the fin efficiency for the two designs, additional simulations were performed with isothermal boundary conditions set on the bottom plate of the heat sink. The imposed temperature corresponds to the value of $T_{\text{in}}+\Delta T_0$ (see Eq. (8)). Subsequently, the fin efficiency was computed as

$$\eta_{\text{fin}} = \frac{q_{\text{fin,cht}}}{q_{\text{fin,max}}}, \tag{13}$$

where $q_{\text{fin,cht}}$ is the heat transfer rate across the fins obtained from CHT simulations and $q_{\text{fin,max}}$ is the heat transfer rate with the fin surfaces at the same temperature of the bottom plate.

The Fanning friction factor can be computed using

$$f = \frac{\Delta P}{\frac{1}{2}\rho V^2_{\text{mean}}} \cdot \frac{D_{\text{h}}}{4\text{L}}, \tag{14}$$

where V_{mean} is the mean velocity in the channel, D_{h} is the hydraulic diameter of the channel and L is the length of the heat sink. Table 4 shows a 24.1% increase in the heat transfer coefficient and an 18.8% decrease in friction factor, in analogy with the obtained reductions of ΔP and ΔT.

The analysis of the thermo-hydraulic performance of the heat sink designs is presented as follows. Firstly, the obtained 3D heat sink geometry, along with the temperature fields, is documented. Then, the shape of the optimized fin is compared to the baseline in terms of various geometric properties. Next, the performance achieved with the optimized heat sink geometry is analyzed and compared to that of the baseline design through heatmaps depicting the local heat transfer rates and heat transfer coefficients. The hydraulic performance is thereafter examined in terms of normalized pressure drop. The thermal–hydraulic analysis is first supported by 2D contours and then corroborated with line plots of the flow properties.

The 3D temperature fields in the solid domains of the baseline and optimized designs are presented in Fig. 7. Additionally, Fig. 7 depicts the velocity contours at representative horizontal ($z_{0.5}$) and vertical planes ($w_{p'}$) in the flow domain. It can be noted that the optimized design leads to a temperature decrease at the bottom solid plate, in particular in correspondence to the root of the fins. Moreover, it can be observed in Fig. 7 that the optimized design features fins with a larger base but a slender profile in the central bulk-flow region (around $\frac{z}{\text{H}} = 0.5$).

The shape of the baseline cylindrical fin and the optimized fin are compared in Fig. 8. Additionally, Fig. 8 depicts the variation of geometric properties, such as the cross-sectional area (a), perimeter (p), and projected frontal length (l_{fr}), with the height of the fin/channel. The optimized fin geometry features a cross-sectional area at the bottom of the fin that is twice that of the baseline cylindrical geometry (see $\frac{a}{a_0}$ subplot in Fig. 8). This increase in the base area results in more heat conduction through the fins given the applied uniform heat flux at the heat sink bottom plate. Moreover, the increased wetted surface of the pin in the bottom region (approximately 40% larger than in the baseline geometry) is beneficial for increasing convective heat transfer. Additionally, the enlarged fin root warrants a higher fin efficiency. Furthermore, the optimized fin exhibits a reduced frontal area (A_{fr}), resulting in less blockage to the flow. This reduction in blockage is most significant around the fin midspan (about $z = 0.4$ H), where l_{fr}, the maximum width of the fin projected normal to the streamwise direction, is about 40% smaller than the baseline.

The fin volume ($\mathcal{V}$), surface area (A_{surf}), and frontal area (A_{fr}) for the optimized geometry are reduced by 10%, 2%, and 14%, respectively, compared to the original cylindrical fin.

Fig. 9 presents the heat transfer rate distribution along the height of the fins through so-called heatmaps. The heatmaps are obtained by dividing the fins into four zones along the span and determining the heat transfer rate in each zone. The optimized geometry achieves a higher heat transfer rate than the baseline in all zones below fin midspan, i.e., below $z_{0.5}$. Conversely, for the region above $z_{0.75}$, the baseline geometry has a higher heat transfer rate, while for the zone between $z_{0.5}$ and $z_{0.75}$, the optimized geometry has a higher heat transfer rate only in the first four fins. The reason is that the bluff-body profile of the upper part of the optimized fins promotes a redistribution of the coolant flow (see Fig. 12 at $w_{0.5}$) towards the heated plate ($0.2 < \frac{z}{\text{H}} < 0.5$), at the expense of a reduction in heat transfer in the upper zones of the fins.

The variation of the local heat transfer coefficient along the fin height is displayed by means of heatmaps generated by averaging the local heat transfer coefficient across the four zones into which the fins are subdivided. The zone-wise heat transfer coefficient is computed by

$$\bar{h}_z = \frac{1}{A_{\text{surf},z}} \int_{A_{\text{surf},z}} \frac{q''}{T - T_{\text{in}}} \, \text{d}A_{\text{surf}}, \tag{15}$$

where q'', T are local heat flux and temperature values, and $A_{\text{surf},z}$ is the surface area corresponding to each zone. Note that the computation of the heat transfer coefficients is performed with the heat flux estimated

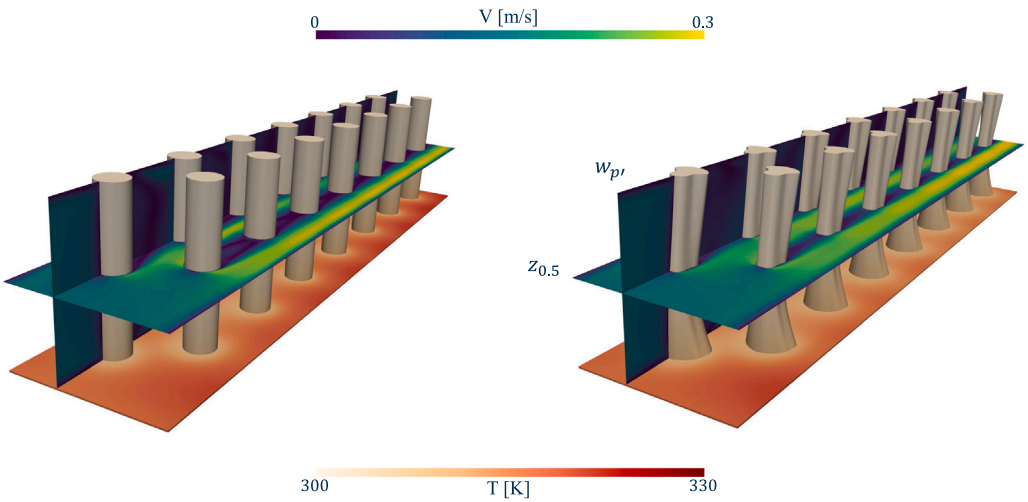

Fig. 7. 3D temperature field contours in the solid domains of the baseline (left) and the optimized (right) designs, with 2D velocity contours at the planes $z_{0.5}$ and $w_{p'}$ in the fluid domains. The plane at $z_{0.5}$ is a horizontal cross-section at half the height of the fin, i.e. $\frac{z}{H} = 0.5$, while the plane $w_{p'}$ is a vertical slice passing through the center of the odd-numbered pins (see Fig. 5).

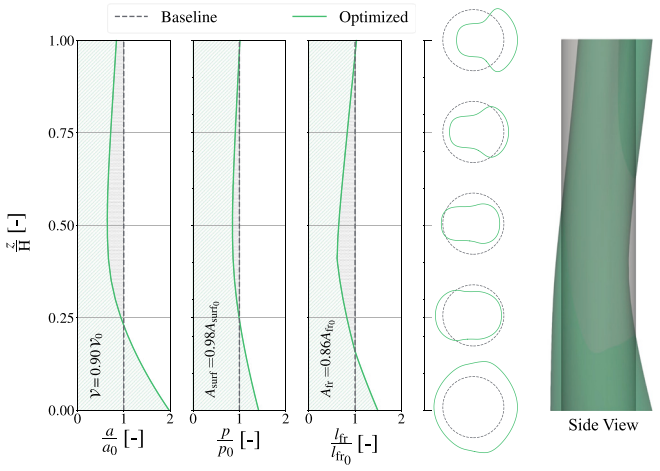

Fig. 8. Variation of the cross-sectional area (a), perimeter (p), projected frontal length (l_{fr}) of the optimized fin along the height, normalized by the baseline values (subscript 0). The integrals of these geometrical quantities over the height correspond to the fin volume ($\mathcal{V}$), surface area (A_{surf}), and frontal area (A_{fr}), respectively. The side view of the baseline and optimized fin geometries is shown on the right.

by means of the simulations with isothermal solid surface used for the computation of $q_{fin,max}$ in Eq. (13). This approach ensures the accuracy of the estimation of the heat transfer coefficient since the effect of fin efficiency is explicitly excluded from the computation. The optimum geometry features higher heat transfer coefficient values than the baseline one in most of the zones below the fin midspan, i.e., below $z_{0.5}$, except in correspondence to the initial pins. Additionally, the heat transfer coefficient at the unfinned base plate is higher than in the baseline design. Since the heat transfer coefficients are higher in the region near the heat source, the heat dissipation is enhanced with the optimized design.

The effect of enhanced heat dissipation is reflected in the temperature distributions presented in Fig. 11. It can be seen from the temperature contours at the bottom heat sink surface (the plane indicated as z_b in the figure) that the optimized design results into a lower average temperature at the base along with a more uniform temperature distribution. The improved performance can be attributed to the following flow features observable in the velocity contours in Fig. 11. Firstly, in correspondence to the central bulk-flow region ($0.25 < \frac{z}{H} < 0.75$), the slender shape of the optimized fin allows the flow to remain attached over a larger extent of the fin profile than in the baseline design (see in Fig. 11 the velocity field at $z_{0.5}$), ultimately enhancing the local heat transfer coefficient. Furthermore, the larger hub profile of the pin leads to more pronounced recirculation zones near the bottom heated region (illustrated by Fig. 11 at $z_{0.1}$). The net effect is the enhancement in flow mixing (see Appendix B), which in turn results in higher heat transfer rates in the bottom part of the pins and a higher heat transfer coefficient along the unfinned part of the base plate (see Figs. 9 and 10). The recirculation zones are also present near the top wall of the channel, as the fin features a bluff-body profile in the aft part. A key benefit of such unconventional pin geometry is the promotion of flow redistribution towards the higher temperature regions (see Fig. 12 at $w_{0.5}$). Finally, the optimized fins are leaned in the z-direction (see the side view in Fig. 8 and w_p in Fig. 12). This leads to a decrease in the frontal area and the associated flow blockage for the same pin wetted area (see also 8).

Hydraulic performance is investigated by computing viscous dissipation across each pin, expressed in terms of non-dimensionalized Euler number (Eu), and comparing it for the two designs in Fig. 13. Eu corresponding to each pin i is computed by

$$Eu_i = \frac{\Delta P_{t,i}}{\frac{1}{2}\rho V_{mean}^2}, \tag{16}$$

where $\Delta P_{t,i}$ is the total pressure drop across the ith pin, ρ is the density of water and V_{mean} is the mean velocity in the channel. The total pressure drop (ΔP_t) across any pin, for example, Pin 11 (see Fig. 5), is computed as

$$\Delta P_{t,11} = P_{(a)} + \frac{1}{2}\rho V_{mean,(a)}^2 - P_{(b)} - \frac{1}{2}\rho V_{mean,(b)}^2, \tag{17}$$

which denotes the difference in average static and dynamic pressure between locations (a) and (b) defined by the cross-sectional planes at the centers of preceding and succeeding pins. Across all pins, the Eu number for the optimized design is consistently lower than that calculated for the baseline geometry, thus indicating lower viscous dissipation. The reduction in pressure drop achieved with the optimized design results from the lower blockage to the flow caused by the fins in the bulk-flow region (around $0.25 < \frac{z}{H} < 0.75$, see $\frac{l_{fr}}{l_{fr_0}}$ subplot in Fig. 8). Furthermore, due to the slender profiles, the flow separation is delayed (see Fig. 12 at $w_{0.5}$), leading to a smaller recirculation zone and, thus, lower mixing losses.

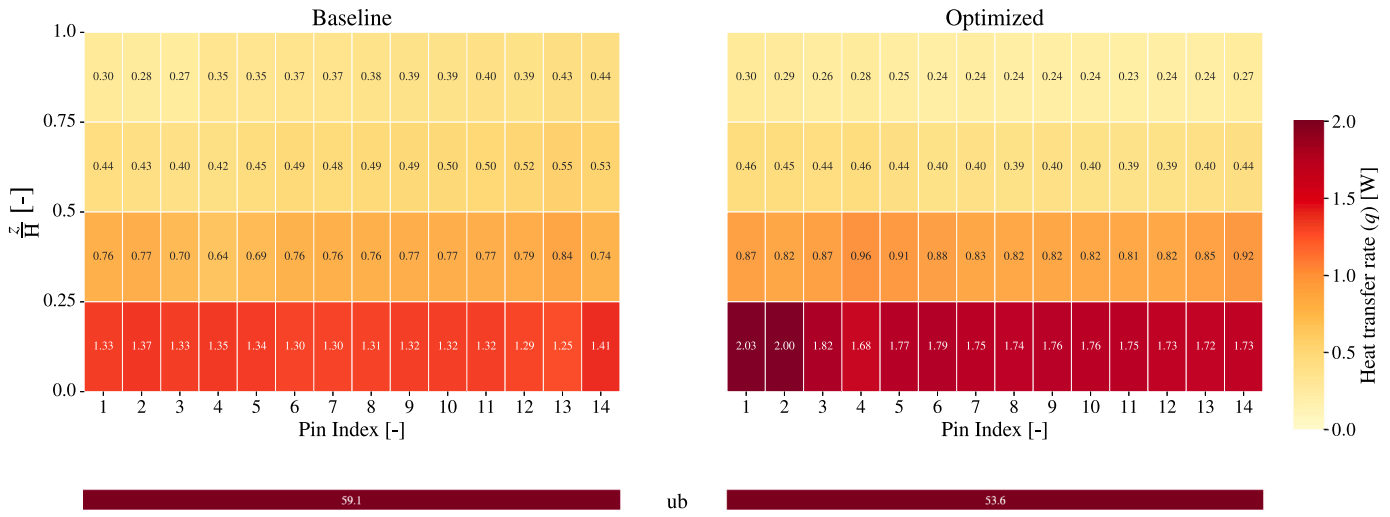

Fig. 9. Comparison of heat transfer rate between the baseline and optimized designs. The heatmaps depict the heat transfer rate along the vertical axis of the fins for both design solutions. Four zones are considered along the fin height. Their extension is defined by the distance between the normalized heights $\frac{z}{H}$ of 0, 0.25, 0.5, 0.75, and 1. The heat transfer rate across the base plate ('ub') is also displayed.

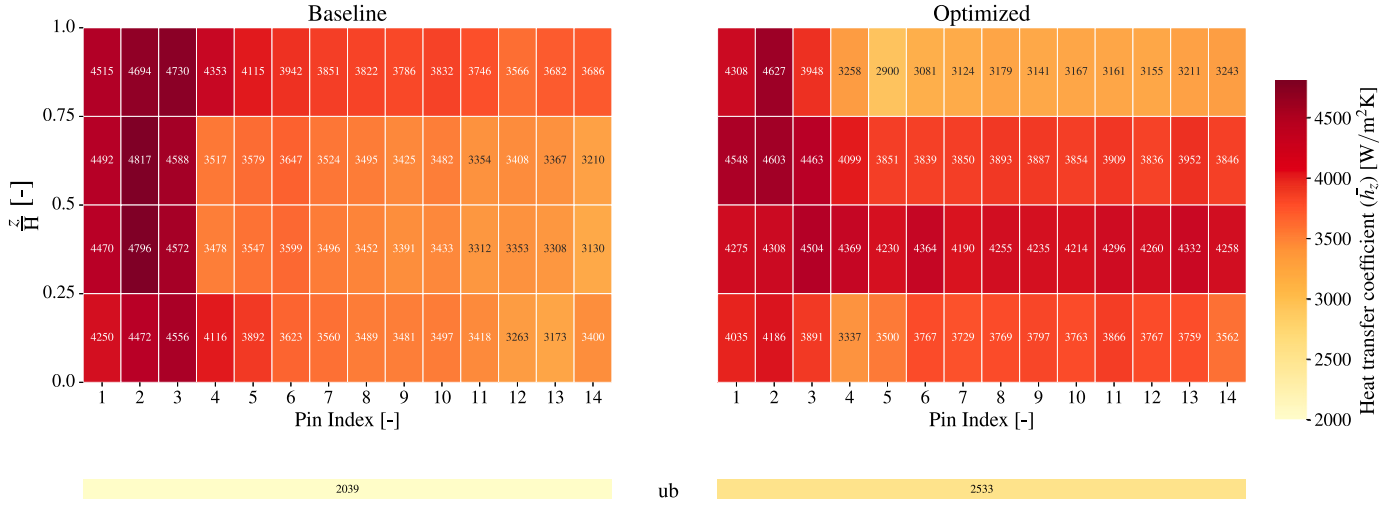

Fig. 10. Comparison of heat transfer coefficients estimated for the baseline and optimized designs along each fin height. The extension of the four zones in which the fins are subdivided is defined by the distance between the normalized heights $\frac{z}{H}$ of 0, 0.25, 0.5, 0.75, and 1. The average heat transfer coefficient at the base plate ('ub') is also displayed.

The trend in the *Eu* number and the improved thermal–hydraulic performance of the optimized design is further corroborated by plotting specific flow properties along the heat sink. The variation of gauge pressure in the streamwise direction is illustrated in Fig. 14. Apart from the inlet region where the entrance effects ($\sim \frac{x}{L} < 0.2$) are prominent, the pressure along the main flow direction features a steady decline, with the optimized design exhibiting a more gradual decrease as a consequence of the better aerodynamic profile of the fins.

The temperature variation along the length of the heat sink at the center of the bottom heated surface is shown in Fig. 14. The optimized design features a more uniform temperature distribution on the heat sink base plate. In contrast, for the baseline design, the temperature rises monotonically along the streamwise direction. The analysis of the temperature variation on the bottom heated surface along an axis passing through the center of the pins (see Fig. 5) reveals that the temperature has large fluctuations, whose period is equal to the longitudinal pin pitch. Notably, the local minima in the temperature distribution correspond to the positions of the pins. Moreover, the fluctuations are more pronounced for the baseline design. In the first pin rows ($\sim \frac{x}{L} < 0.3$), the temperature at the base of the baseline pins is lower than in the case of the optimized design. This is due to the higher average heat transfer coefficient established in the initial part of the heat sink (see Fig. 10), as a result of larger flow accelerations.

Fig. 15 shows the variation of the temperature of the heated surface along the line (a) indicated in Fig. 5, namely along the width of the channel in correspondence to fin 10. At this distance from the entrance, the flow is fully developed for both designs. The temperature of the base plate at location (a) varies in a range of 13 K for the baseline geometry while in an interval of about 7.5 K for the optimized geometry. The lower temperature variation is a consequence of the more uniform temperature distribution achieved with the optimized fin shape.

The plots in Fig. 15 also present the variation of the streamwise velocity component (V_x) along the channel width and at the fin midspan ($z_{0.5}$) in correspondence to the line (a) in Fig. 5. The reduction in V_x observed around $\frac{y}{W} \sim 0.66$ is associated with the location of Pin 9 and its wake. In the case of the baseline design, the velocity becomes negative at $\frac{y}{W} \sim 0.66$. This indicates that the wake region of Pin 9, and, in general, of all the cylindrical fins, extends further in the streamwise direction than in the case of the optimized fins. Moreover, for the

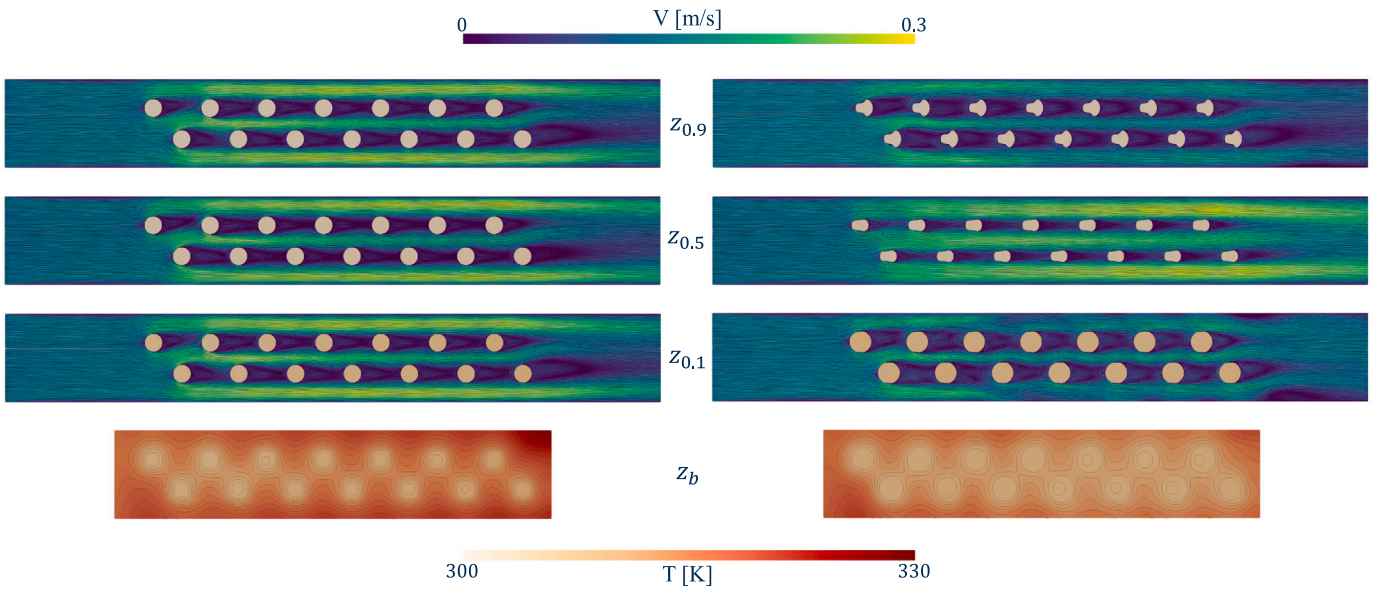

Fig. 11. Comparison of the velocity contours in the fluid domain at selected spanwise cross-sections and the temperature contours in the solid domain at the bottom heated surface (z_b) for the baseline (left) and the optimized (right) designs. The horizontal slices in the fluid domain are taken at normalized heights $\frac{z}{H}$ of 0.9, 0.5, and 0.1.

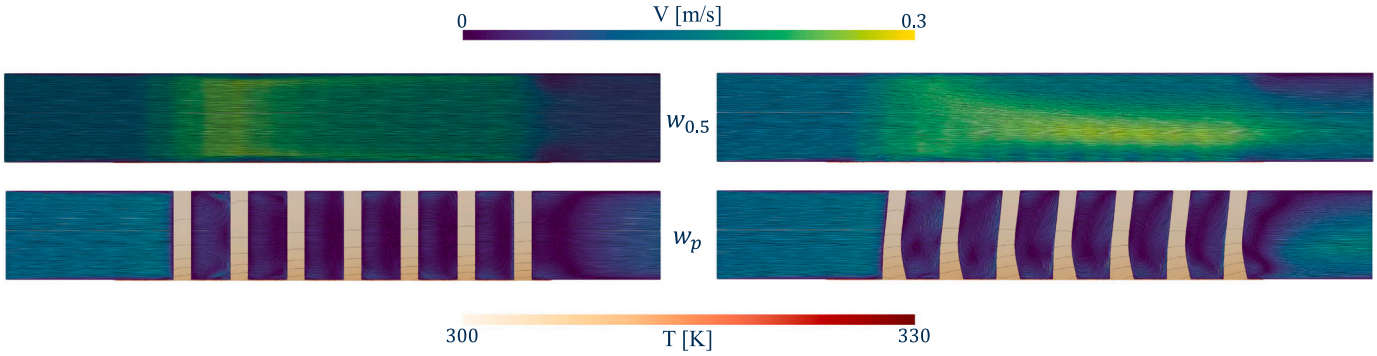

Fig. 12. Comparison of the velocity contours in the fluid domain and the temperature contours in the solid domain at selected vertical cross-sections for the baseline (left) and the optimized (right) designs. The vertical cross-sections are taken at half the channel width ($w_{0.5}$), as well as at a plane w_p passing through the center of the even-numbered pins (see Fig. 5).

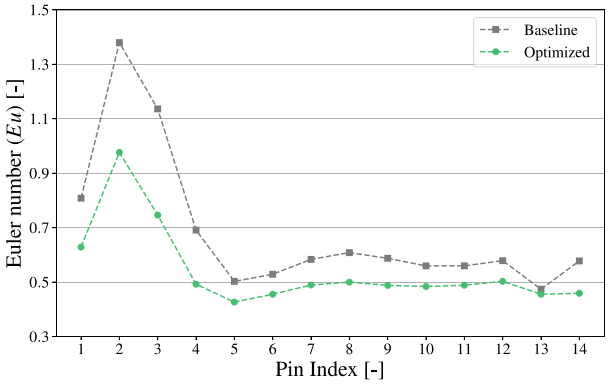

Fig. 13. Comparison of Euler number between the baseline and optimized designs.

optimal design, the average velocity magnitude along the line (a) is higher. This is particularly noticeable near Pin 10, i.e. in the interval $0.2 < \frac{y}{W} < 0.5$. The reason for this difference in the velocity magnitude is twofold. First, the optimized fin features a smaller frontal area at midspan. Second, the coolant mass flow rate is higher at the center of the channel (see Fig. 12 at $w_{0.5}$).

Finally, the temperature distributions along the vertical axis of Pin 2 and Pin 10 are presented in Fig. 16. The plot shows that the temperature distribution in the fins differs only marginally from Pin 2 to Pin 10 for the optimized design, while for the baseline design, the average temperature of the pins increases significantly passing from Pin 2 to Pin 10.

Overall, the optimized fins allow for a lower and more uniform temperature in the heat sink base plate thanks to the higher heat transfer coefficients in the lower half of the fins. This results from a reduction of the fin wake in the bulk-flow region, larger recirculation zones, and then flow mixing near the bottom heated plate, as well as higher flow rates in the lower part of the heat sink. The reduction in pressure drop is due to reduced blockage and delayed separation in the bulk-flow region. In addition, a wider fin base leads to increased fin efficiency. The findings of this study demonstrate that significant improvement in the thermal–hydraulic performance of heat sinks can be achieved with reasonable computational cost using a method that combines adjoint-based shape optimization with CAD-based parametrization.

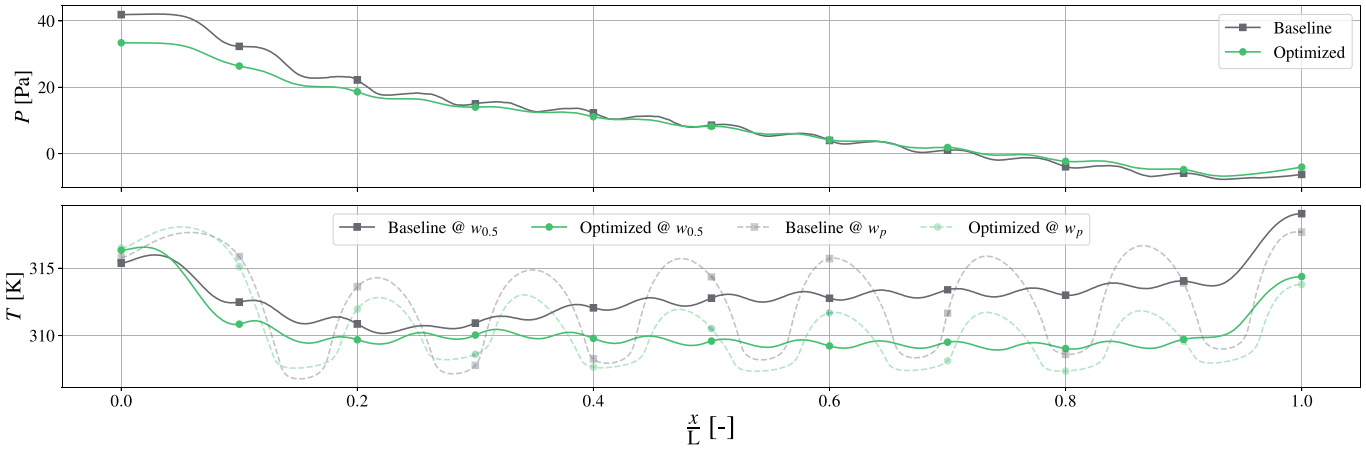

Fig. 14. Pressure and temperature variation along the streamwise direction at specific locations in the fluid and solid domains, respectively. The top plot shows the pressure distribution along a line positioned at mid-height and mid-width of the fluid domain, while the bottom plot presents the temperature distribution at the bottom heated surface at half the width of the channel ($w_{0.5}$), and along a line w_p passing through the centers of even-numbered pins (see Fig. 5).

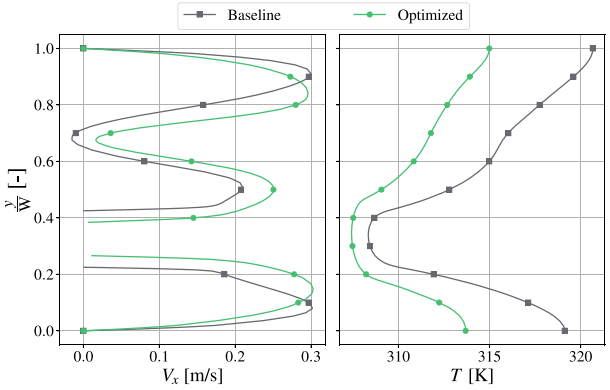

Fig. 15. Velocity and temperature distributions at lines normal to the streamwise direction in the fluid and solid domains at the location of Pin 10 (see line (a) in Fig. 5). The velocity distribution is sampled at $z_{0.5}$ while the temperature distribution corresponds to the bottom heated surface z_b.

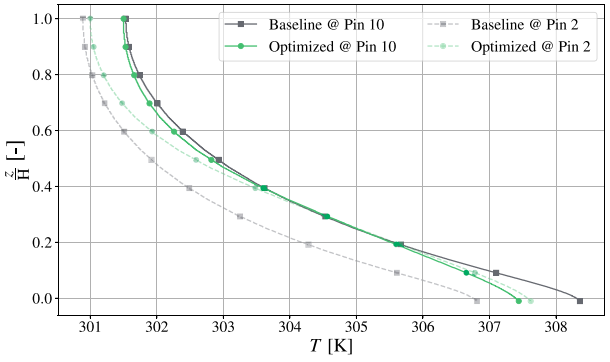

Fig. 16. Temperature distributions along the vertical axis of Pin 10 and Pin 2 (see Fig. 5).

5. Conclusions

The research work documented in this paper focused on the development of a method to perform shape optimization for conjugate heat transfer problems using the adjoint method and CAD-based parametrization. The design framework, comprising the open-source CFD software SU2 [26] with adjoint capabilities and a CAD-based parametrization tool [27] was applied to optimize the shape of the fins of a water-cooled heat sink.

The main conclusions of the work can be summarized as follows.

1. The optimization resulted in an unconventional fin geometry, enabling an increase in the average heat transfer coefficient by 23.3% while reducing the pressure drop by 18.8%, compared to the original cylindrical fins.
2. The optimized fins feature a larger cross-section at the hub, leading to more heat conduction through the pins, and a slender profile in the 25%–75% range of the span, enhancing convective heat transfer and minimizing flow blockage.
3. The improvement in the thermo-hydraulic performance of the heat sink is achieved also through a redistribution of the flow towards the heated base plate.
4. Though the design method proved to be robust and enabled the attainment of unconventional fin shapes, further improvements can be envisaged if the current limitations of the adopted mesh deformation method to handle large grid displacements will be addressed.

This study demonstrates the capability of the method in generating innovative designs for fins. Future work will focus on incorporating a more sophisticated mesh deformation based on radial basis functions and applying the design framework to cases with non-uniform heat flux. In addition, the use of local sensitivities to optimize the individual fin shapes will be explored.

CRediT authorship contribution statement

Praharsh Pai Raikar: Writing – original draft, Methodology, Investigation, Conceptualization. **Nitish Anand:** Writing – review & editing, Supervision, Methodology, Conceptualization. **Matteo Pini:** Writing – review & editing, Supervision, Methodology, Conceptualization. **Carlo De Servi:** Writing – review & editing, Supervision, Methodology, Funding acquisition, Conceptualization.

Declaration of competing interest

The authors declare that they have no known competing financial interests or personal relationships that could have appeared to influence the work reported in this paper.

Acknowledgments

The research reported in this manuscript was funded by the Vlaamse Instelling voor Technologisch Onderzoek (VITO), Belgium, through project number 2010489. The computational resources and services used in this work were provided by the HPC core facility CalcUA of the Universiteit Antwerpen, and VSC (Flemish Supercomputer Center), funded by the Research Foundation - Flanders (FWO) and the Flemish Government. The authors are also grateful to Prof. P. Colonna for his valuable comments during the development of this study.

Appendix A. Gradient verification

The gradients obtained using the design chain with the adjoint (ADJ) method are verified by comparing their values with those obtained by the finite-difference (FD) method. The approach for gradient verification was similar to the one in Ref. [25], properly adapted to account for the 3D parametrization and multi-zone domains. The gradient verification was performed for a reduced set of design variables due to the high computational cost associated with the 3D CHT simulations. Among the randomly selected 50 design variables were thickness parameters defining the pin profile in both the freestream flow in the wake regions. Based on a preliminary parametric study, two FD step sizes, 0.1% and 0.05%, were selected for the computation of gradients using FD. Fig. A.17 presents the comparison of the values of the gradient of the objective function computed using the adjoint methods and the FD step size that resulted in the best quantitative agreement. Using this approach, the average deviation obtained for most variables was less than 5%. For the purpose of the optimization case study, the extent of the deviations observed in Fig. A.17 is considered adequate.

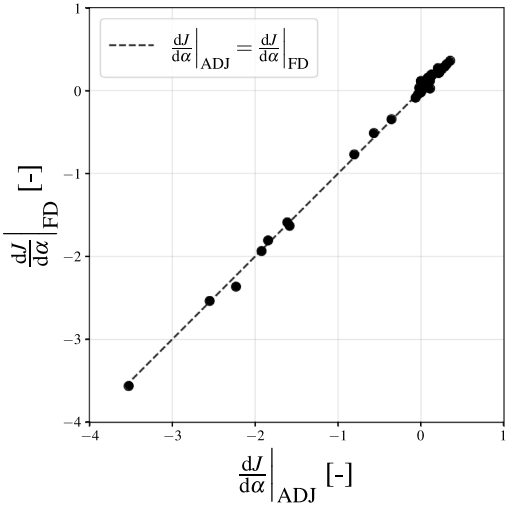

Fig. A.17. Gradient verification plot for the design variables of the case study.

Appendix B. Quantification of mixing in recirculation zones

The mixing in recirculation zones near the heated bottom plate in the optimized design is quantified in terms of standard deviation and coefficient of variance of temperature. Lower values of these quantities indicate a more homogeneous temperature field in the fluid caused by improved mixing. The coefficient of variation of temperature in a control volume is given by:

$$COV_T = \frac{\sigma_T}{\bar{T}}, \tag{B.1}$$

where $\bar{T}$ is the volume-average temperature and σ_T is standard deviation computed by

$$\sigma_T = \sqrt{\frac{1}{V}\int_V (T-\bar{T})^2 \, dV}. \tag{B.2}$$

To analyze the mixing associated with the recirculation zones near the heated bottom plate (depicted by the velocity contours in Fig. 11 at $z_{0.1}$), control volumes are selected in the wake of Pin 2 and Pin 10. The control volumes, represented in Fig. B.18, span from the bottom heated surface (z_b) to $z_{0.1}$. The computed parameters corresponding to the baseline and optimized designs are reported in Table B.5.

The optimized geometry leads to more than ~60% reduction in σ_T and COV_T values compared to the baseline design. This is because the optimized design promotes mixing and leads to more homogeneous fluid temperatures in the analyzed region.

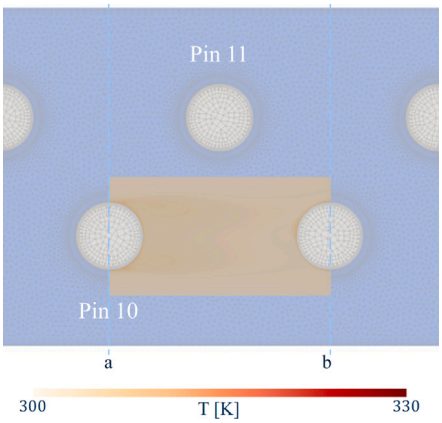

Fig. B.18. Representation of the control volume selected for quantification of mixing in the wake corresponding to Pin 10 (see Fig. 5) along with its temperature distribution. The control volume spans from the bottom heated surface z_b to $z_{0.1}$.

Table B.5
Comparison of volume-averaged temperature ($\bar{T}$), standard deviation (σ_T), and coefficient of variation (COV_T) in the wake regions behind the Pin 2 and Pin 10 for the baseline and optimized geometries.

Metric	Baseline		Optimized	
	Pin 2	Pin 10	Pin 2	Pin 10
$\bar{T}$ [K]	302.39	303.12	302.10	302.11
σ_T [K]	8.59	8.58	2.38	2.05
COV_T	0.0284	0.0283	0.0079	0.0068

Data availability

Data will be made available on request.

References

[1] B.J. Brelje, J.R. Martins, Electric, hybrid, and turboelectric fixed-wing aircraft: A review of concepts, models, and design approaches, Prog. Aerosp. Sci. 104 (2019) 1–19, http://dx.doi.org/10.1016/j.paerosci.2018.06.004.

[2] M. Asli, P. König, D. Sharma, E. Pontika, J. Huete, K.R. Konda, A. Mathiazhagan, T. Xie, K. Höschler, P. Laskaridis, Thermal management challenges in hybrid-electric propulsion aircraft, Prog. Aerosp. Sci. 144 (2024) 100967, http://dx.doi.org/10.1016/j.paerosci.2023.100967.

[3] M. Coutinho, D. Bento, A. Souza, R. Cruz, F. Afonso, F. Lau, A. Suleman, F.R. Barbosa, R. Gandolfi, W.A. Junior, et al., A review on the recent developments in thermal management systems for hybrid-electric aircraft, Appl. Therm. Eng. 227 (2023) 120427, http://dx.doi.org/10.1016/j.applthermaleng.2023.120427.
[4] H.E. Ahmed, B. Salman, A.S. Kherbeet, M. Ahmed, Optimization of thermal design of heat sinks: A review, Int. J. Heat Mass Transfer 118 (2018) 129–153, http://dx.doi.org/10.1016/j.ijheatmasstransfer.2017.10.099.
[5] M.M.A. Bhutta, N. Hayat, M.H. Bashir, A.R. Khan, K.N. Ahmad, S. Khan, CFD applications in various heat exchangers design: A review, Appl. Therm. Eng. 32 (2012) 1–12, http://dx.doi.org/10.1016/j.applthermaleng.2011.09.001.
[6] Y. Wang, L.-C. Wang, Z.-M. Lin, Y.-H. Yao, L.-B. Wang, The condition requiring conjugate numerical method in study of heat transfer characteristics of tube bank fin heat exchanger, Int. J. Heat Mass Transfer 55 (9–10) (2012) 2353–2364, http://dx.doi.org/10.1016/j.ijheatmasstransfer.2012.01.029.
[7] M. Ahmadian-Elmi, A. Mashayekhi, S. Nourazar, K. Vafai, A comprehensive study on parametric optimization of the pin-fin heat sink to improve its thermal and hydraulic characteristics, Int. J. Heat Mass Transfer 180 (2021) 121797, http://dx.doi.org/10.1016/j.ijheatmasstransfer.2021.121797.
[8] M. Kim, M.Y. Ha, J.K. Min, A numerical study on various pin–fin shaped surface air–oil heat exchangers for an aero gas-turbine engine, Int. J. Heat Mass Transfer 93 (2016) 637–652, http://dx.doi.org/10.1016/j.ijheatmasstransfer.2015.10.035.
[9] K. Hu, C. Lu, B. Yu, L. Yang, Y. Rao, Optimization of bionic heat sinks with self-organized structures inspired by termite nest morphologies, Int. J. Heat Mass Transfer 202 (2023) 123735, http://dx.doi.org/10.1016/j.ijheatmasstransfer.2022.123735.
[10] N.P. Nguyen, E. Maghsoudi, S.N. Roberts, B. Kwon, Shape optimization of pin fin array in a cooling channel using genetic algorithm and machine learning, Int. J. Heat Mass Transfer 202 (2023) 123769, http://dx.doi.org/10.1016/j.ijheatmasstransfer.2022.123769.
[11] C. Yu, X. Zhu, Z. Li, Y. Ma, M. Yang, H. Zhang, Optimization of elliptical pin-fin microchannel heat sink based on artificial neural network, Int. J. Heat Mass Transfer 205 (2023) 123928, http://dx.doi.org/10.1016/j.ijheatmasstransfer.2023.123928.
[12] M.E. Polat, S. Cadirci, Artificial neural network model and multi-objective optimization of microchannel heat sinks with diamond-shaped pin fins, Int. J. Heat Mass Transfer 194 (2022) 123015, http://dx.doi.org/10.1016/j.ijheatmasstransfer.2022.123015.
[13] J. Nocedal, S.J. Wright, Numerical Optimization, second ed., in: Springer Series in Operations Research and Financial Engineering, Springer, New York, 2006, http://dx.doi.org/10.1007/978-0-387-40065-5.
[14] K. Gkaragkounis, E. Papoutsis-Kiachagias, K. Giannakoglou, The continuous adjoint method for shape optimization in conjugate heat transfer problems with turbulent incompressible flows, Appl. Therm. Eng. 140 (2018) 351–362, http://dx.doi.org/10.1016/j.applthermaleng.2018.05.054.
[15] K.T. Gkaragkounis, E.M. Papoutsis-Kiachagias, K.C. Giannakoglou, Adjoint-assisted Pareto front tracing in aerodynamic and conjugate heat transfer shape optimization, Comput. Fluids 214 (2021) 104753, http://dx.doi.org/10.1016/j.compfluid.2020.104753.
[16] J.L. Anibal, C.A. Mader, J.R. Martins, Aerodynamic shape optimization of an electric aircraft motor surface heat exchanger with conjugate heat transfer constraint, Int. J. Heat Mass Transfer 189 (2022) 122689, http://dx.doi.org/10.1016/j.ijheatmasstransfer.2022.122689.
[17] O. Burghardt, P. Gomes, T. Kattmann, T.D. Economon, N.R. Gauger, R. Palacios, Discrete adjoint methodology for general multiphysics problems: A modular and efficient algorithmic outline with implementation in an open-source simulation software, Struct. Multidiscip. Optim. 65 (2022) 28, http://dx.doi.org/10.1007/s00158-021-03117-5.
[18] P. He, C. Psenica, L. Fang, M. Leader, Aerothermal shape optimization of actively-cooled battery packs using conjugate heat transfer, in: AIAA SCITECH 2025 Forum, American Institute of Aeronautics and Astronautics, 2025, http://dx.doi.org/10.2514/6.2025-1559.
[19] S. Vitale, M. Pini, P. Colonna, Multistage turbomachinery design using the discrete adjoint method within the open-source software SU2, J. Propuls. Power 36 (3) (2020) 465–478, http://dx.doi.org/10.2514/1.B37685.
[20] L. Mueller, T. Verstraete, CAD integrated multipoint adjoint-based optimization of a turbocharger radial turbine, Int. J. Turbomach. Propuls. Power 2 (3) (2017) http://dx.doi.org/10.3390/ijtpp2030014.
[21] N. Anand, S. Vitale, M. Pini, P. Colonna, Assessment of FFD and CAD-based shape parametrization methods for adjoint-based turbomachinery shape optimization, in: Proceedings of Global Power and Propulsion Society, Montreal, Canada, 2018, pp. 1–8, http://dx.doi.org/10.5281/zenodo.1344595.
[22] S. Xu, D. Radford, M. Meyer, J.-D. Müller, CAD-based adjoint shape optimisation of a one-stage turbine with geometric constraints, in: Proceeding of Turbo Expo: Power for Land, Sea, and Air, Volume 2C: Turbomachinery, 2015, V02CT45A006, http://dx.doi.org/10.1115/GT2015-42237.
[23] M. Chávez-Modena, L.M. González, E. Valero, Numerical optimization of the fin shape experiments of a heat conjugate problem surface air/oil heat exchanger (SACOC), Int. J. Heat Mass Transfer 182 (2022) 121971, http://dx.doi.org/10.1016/j.ijheatmasstransfer.2021.121971.
[24] O.R. Imam-Lawal, Adjoint Based Optimisation for Coupled Conjugate Heat Transfer (Ph.D. thesis), Queen Mary University of London, 2020, URL https://qmro.qmul.ac.uk/xmlui/handle/123456789/68283.
[25] P. Pai Raikar, N. Anand, M. Pini, C. De Servi, Concurrent optimization of multiple heat transfer surfaces using adjoint-based optimization with a CAD-based parametrization, Int. J. Heat Mass Transfer 236 (2025) 126230, http://dx.doi.org/10.1016/j.ijheatmasstransfer.2024.126230.
[26] T.D. Economon, F. Palacios, S.R. Copeland, T.W. Lukaczyk, J.J. Alonso, SU2: An open-source suite for multiphysics simulation and design, AIAA J. 54 (3) (2016) 828–846, http://dx.doi.org/10.2514/1.J053813.
[27] R. Agromayor, N. Anand, J.D. Muller, M. Pini, L.O. Nord, A unified geometry parametrization method for turbomachinery blades, Comput. Aided Des. 133 (102987) (2021) 1–16, http://dx.doi.org/10.1016/j.cad.2020.102987.
[28] Various Authors, Parablade, 2020, http://dx.doi.org/10.5281/zenodo.3894778.
[29] P.E. Gill, W. Murray, M.A. Saunders, SNOPT: An SQP algorithm for large-scale constrained optimization, SIAM Rev. 47 (1) (2005) 99–131, http://dx.doi.org/10.1137/S0036144504446096.
[30] N. Wu, G. Kenway, C.A. Mader, J. Jasa, J.R.R.A. Martins, PyOptSparse: A python framework for large-scale constrained nonlinear optimization of sparse systems, J. Open Source Softw. 5 (54) (2020) 2564, http://dx.doi.org/10.21105/joss.02564.
[31] R. Dwight, Robust mesh deformation using the linear elasticity equations, in: Computational Fluid Dynamics 2006, 2009, pp. 401–406, http://dx.doi.org/10.1007/978-3-540-92779-2_62.
[32] L. Piegl, W. Tiller, The NURBS Book, second ed., Springer Science & Business Media, 2012, http://dx.doi.org/10.1007/978-3-642-59223-2.
[33] T. Kattmann, Efficient Adjoint-Based Design Capability for Unsteady Conjugate Heat Transfer Problems (Ph.D. thesis), Rheinland-Pfälzische Technische Universität Kaiserslautern-Landau, 2025, p. XIV, 131, http://dx.doi.org/10.26204/KLUEDO/9056.
[34] T.D. Economon, Simulation and adjoint-based design for variable density incompressible flows with heat transfer, AIAA J. 58 (2) (2020) 757–769, http://dx.doi.org/10.2514/1.J058222.
[35] M. Sagebaum, T. Albring, N.R. Gauger, High-performance derivative computations using CoDiPack, ACM Trans. Math. Software 45 (4) (2019) http://dx.doi.org/10.1145/3356900.
[36] R. Sanchez, T. Albring, R. Palacios, N.R. Gauger, T.D. Economon, J.J. Alonso, Coupled adjoint-based sensitivities in large-displacement fluid-structure interaction using algorithmic differentiation, Internat. J. Numer. Methods Engrg. 113 (7) (2017) 1081–1107, http://dx.doi.org/10.1002/nme.5700.
[37] O. Burghardt, N.R. Gauger, T.D. Economon, Coupled adjoints for conjugate heat transfer in variable density incompressible flows, in: AIAA (2019–2668), 2019, http://dx.doi.org/10.2514/6.2019-3668.
[38] P. He, C.A. Mader, J.R. Martins, K.J. Maki, Aerothermal optimization of a ribbed U-bend cooling channel using the adjoint method, Int. J. Heat Mass Transfer 140 (2019) 152–172, http://dx.doi.org/10.1016/j.ijheatmasstransfer.2019.05.075.
[39] I. Pointwise, Pointwise, 2022, https://www.pointwise.com. [Computer software].
[40] N.P. Nguyen, E. Maghsoudi, S.N. Roberts, D.C. Hofmann, B. Kwon, Understanding heat transfer and flow characteristics of additively manufactured pin fin arrays through laser-induced fluorescence and particle image velocimetry, Int. J. Heat Mass Transfer 222 (2024) 125198, http://dx.doi.org/10.1016/j.ijheatmasstransfer.2024.125198.